Journal of Materials Chemistry A

ROYAL SOCIETY OF CHEMISTRY

PAPER

View Article Online
View Journal

Cite this: DOI: 10.1039/d6ta01264g

Two-dimensional mercury(II)–acetylide framework with built-in dipole field for efficient photocatalytic CO_2-to-CO conversion

Mude Zhu,[ac] Muchun Xu,[a] Lincan Fang*[b] and Linli Xu *[ac]

The development of efficient photocatalysts for CO_2 reduction remains a critical challenge in artificial photosynthesis. While two-dimensional (2D) coordination frameworks provide structural versatility, the catalytic potential of main-group metal-containing frameworks is still largely underexplored. Herein, we report a semicrystalline 2D Hg^{II}–acetylide framework featuring linear –C≡C–Hg–C≡C– motifs, which exhibits exceptional photocatalytic activity and selectivity for CO_2-to-CO conversion. Density functional theory (DFT) analysis reveals anisotropic orbital hybridization within these motifs, wherein Hg $5d_\pi$ orbitals engage in backbonding with alkynyl π^* systems, creating an electron-deficient catalytic interface precisely tailored for CO_2 activation. Importantly, the asymmetric electron distribution across each –C≡C–Hg– unit generates a strong local dipole moment that aligns coherently throughout the framework, establishing a macroscopic built-in electric field. This field functions as an internal charge pump under vibration, dramatically enhancing photogenerated carrier separation and directing electrons toward the metal–acetylide active sites. The synergy between orbital hybridization and dipole-driven charge transfer enables efficient CO_2 adsorption/activation and rapid *CO desorption, achieving a CO evolution rate of 338.57 μmol g^{-1} h^{-1} with 65% selectivity, along with 30.15 μmol g^{-1} h^{-1} of CH_4 in the presence of triethanolamine (TEOA) and sacrificial agents during photocatalytic performance under ultrasonic vibration, highlighting the kinetic advantages conferred by the field-driven mechanism. This work demonstrates dipole engineering in main-group metal–acetylide frameworks as a generalizable strategy for designing high-performance photocatalytic materials.

Received 10th February 2026
Accepted 4th May 2026

DOI: 10.1039/d6ta01264g

rsc.li/materials-a

Linli Xu

Linli Xu is an assistant professor in the Department of Applied Biology and Chemical Technology at the Hong Kong Polytechnic University (PolyU). She obtained her PhD degree in 2010 from Guangzhou Institute of Chemistry, Chinese Academy of Sciences (CAS). She worked as a postdoctoral fellow and assistant researcher at the Technical Institute of Physics and Chemistry (IPC), CAS, from 2010 to 2017. Then she moved to PolyU as a research fellow and research assistant professor from 2017 to 2023. Her research focuses on developing 2D carbon and carbon-rich materials and their applications in optoelectronics, energy science and thermal management.

1. Introduction

The photocatalytic conversion of CO_2 into value-added chemical fuels offers a promising strategy for carbon cycling and sustainable energy production. However, realizing this potential requires photocatalysts that simultaneously achieve efficient light harvesting, rapid charge separation, selective CO_2 activation, and stable product desorption—particularly for CO as the target product.[1,2] 2D coordination frameworks have emerged as ideal platforms,[3,4] combining molecular-level synthetic precision with extended charge delocalization pathways inherent to solid-state materials.[4,5]

Among these, 2D metal–acetylide frameworks (MAFs) constructed *via* linear –C≡C–M–C≡C– (M = Hg^{II}, Ni^{II}, Pd^{II}, Pt^{II}) linkages stand out due to their exceptional chemical robustness and π-conjugated backbones that facilitate long-range charge transport.[6–8] A distinguishing feature is the tunable local dipole arising from the metal–acetylide bond polarity,[9] which generates built-in electric fields (BIEFs) that suppress

[a]Department of Applied Biology and Chemical Technology and Research Institute for Smart Energy, The Hong Kong Polytechnic University, Hung Hom, Kowloon, Hong Kong SAR, P. R. China. E-mail: linli.xu@polyu.edu.hk; lincan.fang@ahnu.edu.cn

[b]Key Laboratory of Functional Molecular Solids Ministry of Education, College of Chemistry and Materials Science, Anhui Normal University, Wuhu, Anhui, 241002, P. R. China

[c]PolyU Shenzhen Research Institute, Shenzhen, 518057, P. R. China

charge recombination by spatially separating photogenerated electrons and holes. Our group has previously demonstrated that Ni^{II}-, Pt^{II}-, and Pd^{II}–acetylide frameworks deliver outstanding photocatalytic CO_2 reduction performance.[10–13] Hg^{II}, however, represents an underexplored frontier within this family. Its d^{10} closed-shell configuration and preference for linear two-coordinate geometry, represents a frontier in this exploration. The linear coordination geometry enable strong σ-overlap between Hg (6s and $6p_z$) and sp-hybridized alkynyl carbons,[14] yielding pronounced Hg–C bond polarity.[15] This polarity establishes powerful local dipoles that coherently align across the framework, creating macroscopic BIEFs for efficient carrier extraction to catalytic sites.[16,17] Critically, the extended Hg $5d_\pi$ orbitals (d_{xz}, d_{yz}) engage in lateral d_π–p_π backbonding within the perpendicular π* system of the –C≡C– units.[18] This interaction not only populates the antibonding alkynyl orbitals but also modulates the electron density at the Hg center, thereby optimizing CO_2 adsorption and activation while preventing excessive *CO binding—a common limitation in many transition-metal catalysts. The synergistic combination of such orbital hybridization with BIEF-directed charge flow creates a precisely engineered subnanometer active interface, ideally configured for selective CO_2-to-CO photoconversion.[19–21]

Nevertheless, the static nature of a structurally derived BIEFs can still be constrained by bulk charge recombination and insufficient carrier injection kinetics under operational conditions.[22] A pivotal strategy to overcome this limitation involves dynamically enhancing the material's polarization through external physical stimuli.[23] Introducing mechanical perturbation, such as ultrasound, can not only improve mass transfer but also, more critically, induce periodic lattice strain or dipole reorientation in polar-active materials.[24,25] For instance, in the HETP-Ni-AF framework featuring a strong BIEF, the CO production rate under light irradiation alone is 2.28 μmol g^{-1} h^{-1}, while under combined light and ultrasonic irradiation, it surges remarkably to 129.80 μmol g^{-1} h^{-1}. This dramatic enhancement underscores a synergistic interplay between the intrinsic BIEFs and the ultrasonic perturbation.[8] Such external-field coupling can amplify the pre-existing built-in electric fields, thereby further boost charge-separation efficiency and offering a direct mechanistic probe into the field-driven contribution in photocatalysis.[26]

Herein, we report the synthesis of a novel semicrystalline 2D Hg^{II}–acetylide framework, designated TTED-Hg-AF, which integrates Hg^{II} centers into a graphdiyne-type scaffold derived from 2,7,10,15-tetrakis(ethynyl)dibenzo[*g*,*p*]chrysene (TTED). The rigid, π-extended TTED core enhances in-plane charge delocalization, while the asymmetric –C≡C–Hg–C≡C– motifs generate coherently aligned dipole arrays.[27] Under light irradiation alone, TTED-Hg-AF achieves a photocatalytic CO production rate of 1.60 μmol g^{-1} h^{-1} with 100% selectivity. Strikingly, under simultaneous light and ultrasound irradiation, the CO evolution rate reaches 338.57 μmol g^{-1} h^{-1} with 65% selectivity, accompanied by CH_4 production at 30.15 μmol g^{-1} h^{-1} in the presence of TEOA and a proton source $[Ru(bpy)_3]Cl_2$ (PS). We attribute this exceptional performance to the ultrasound-induced enhancement of the framework's dipole polarization, which vectorially directs electrons to the surface-exposed –C≡C–Hg–C≡C– active sites while funneling holes into the conjugated organic backbone. DFT calculations corroborate that the d_π–p_π backbonding optimally balances the energetics of CO_2 activation and *CO desorption.[28,29] This work establishes main-group metal–acetylide frameworks with strategically engineered dipole fields as a new materials platform for high-performance photocatalysis, providing clear design principles for the development of polarization-driven 2D catalytic systems.

2. Experimental section

2.1 Synthesis of TTED-Hg-AF

TTED-Hg-AF was synthesized *via* a base-catalyzed dehydrohalogenation between the organic ligand TTED and $HgCl_2$ (Scheme 1). The bulk material was prepared using a one-pot solvothermal approach. In a typical procedure, a tetrahydrofuran (THF) solution (1.0 mM) of TTED and a methanol (CH_3OH) solution (2.0 mM) of $HgCl_2$ were combined in a 50 mL Schlenk tube equipped with a magnetic stir bar. The system was degassed by three freeze–pump–thaw cycles (25 min each) to remove dissolved O_2. The reaction mixture was then heated stepwise at 30 °C for 24 h, 60 °C for 24 h, and finally 80 °C for 24 h. For comparison, a mercury-free analogue (TTED-GDY) was synthesized by reacting TTED with CuI in pyridine at 80 °C for 72 h. The resulting solid products were collected by vacuum filtration and purified *via* Soxhlet extraction sequentially with CH_3OH, acetonitrile, and THF for 24 h each to remove unreacted monomers, oligomers, and residual metal salts.

2.2 Characterization

Morphology and elemental composition were examined using scanning electron microscopy (SEM) and energy-dispersive X-ray spectroscopy (EDS) on a Tescan CLARA microscope. Transmission electron microscopy (TEM) and high-resolution TEM (HRTEM) were performed on a JEOL JEM-2100F instrument. Powder X-ray diffraction (PXRD) patterns were collected on a Rigaku SmartLab 9 kW diffractometer over a 2θ range of 5°–40° at a scan rate of 2° min^{-1}. X-ray photoelectron spectroscopy (XPS) measurements were conducted using a Thermo Scientific Escalab 250XI system with Al Kα radiation (12 kV, 6 mA) under ultra-high vacuum (2.0×10^{-7} mbar), and all binding energies were calibrated to the C 1s peak at 284.8 eV. Nitrogen adsorption–desorption isotherms were measured using a BSD660a surface-area and porosimetry analyzer. Prior to analysis, the sample was degassed under vacuum at 80 °C for at least 3 hours to remove adsorbed moisture and contaminants, causing weight loss of 6.75 wt%. Isotherms were recorded at liquid-nitrogen temperature (77 K), and the specific surface area was calculated using the Brunauer–Emmett–Teller (BET) method in the relative pressure (P/P_0) range of 0.03–0.15.

Fourier transform infrared (FTIR) spectra were acquired on a Thermo Nicolet IS50 spectrometer from 4000–600 cm^{-1} with a resolution of 0.2 cm^{-1}. Solid-state ^{13}C cross-polarization

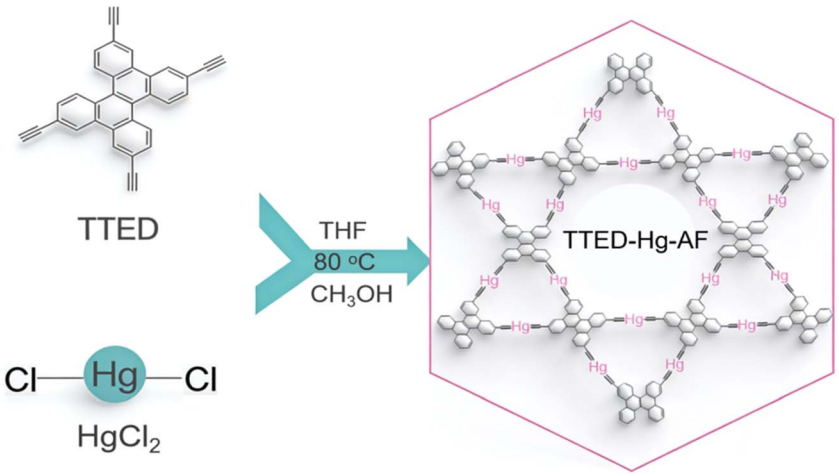

Scheme 1 Synthetic route of TTED-Hg-AF *via* base-catalyzed dehydrohalogenation between $HgCl_2$ and TTED ligand.

magic-angle spinning nuclear magnetic resonance (CP-MAS NMR) spectra were obtained on a JEOL ECZ500R 500 MHz spectrometer. Piezoelectric force microscopy (PFM) and Kelvin probe force microscopy (KPFM) were performed on a Bruker Multimode 8 system. Electrochemical measurements were conducted using a CHI660E workstation. *In situ* high-pressure photoluminescence (PL) spectroscopy employed a custom-built system combining an optical-fiber spectrometer with a Nicolet iN10 microscope spectrometer (Thermo Fisher Scientific). PL spectra of TTED-Hg-AF aqueous suspensions were recorded under 350 nm excitation using an Agilent G9800A Cary Eclipse spectrofluorometer. *In situ* diffuse reflectance infrared Fourier-transform spectroscopy (DRIFTS) was performed on a Thermo Fisher IS50 TKA-7070 setup. Ultraviolet-visible diffuse reflectance spectroscopy (UV-vis DRS) data were collected with a Shimadzu UV-3600i Plus spectrophotometer. Thermogravimetric analysis (TGA) was conducted using a Mettler Toledo TGA/DSC3+ instrument. Gaseous products (CO and H_2) were quantified using a gas chromatograph (SHIMADZU GC-2030). Isotope-labeling experiments with $^{13}CO_2$ were analyzed by gas chromatography-mass spectrometry (GC-MS, SHIMADZU QP-2020 NX).

2.3 Photocatalytic CO_2 reduction

Photocatalytic CO_2 reduction was performed in a sealed 10 mL vial containing 4.2 mL of a mixed solvent (H_2O/triethanolamine = 4 : 0.2 by volume), 1.0 mg of catalyst, and 6.5 mg (0.015 mmol) of $[Ru(bpy)_3]Cl_2$ as photosensitizer. The solution was purged with CO_2 for 30 min prior to irradiation. The reaction was then conducted under simultaneous illumination from a 300 W Xe lamp (λ > 420 nm, 100 mW cm^{-2}) and agitation by a 100 W ultrasonic probe. The temperature was maintained at 26 ± 1 °C using a circulating water bath.

Gaseous products were sampled from the headspace every 0.5 h with a gas-tight Hamilton syringe and analyzed online by gas chromatography equipped with a flame ionization detector (FID) and a thermal conductivity detector (TCD) for quantification of CO, CH_4, and H_2.

3. Results and discussion

3.1 Structural characterization

The chemical structure of TTED-Hg-AF was verified through solid-state ^{13}C CP-MAS NMR, XPS, and FTIR spectroscopy. The solid-state ^{13}C CP-MAS NMR spectrum (Fig. 1a) exhibits characteristic resonances at approximately 85 ppm corresponding to the sp-hybridized –C≡C– carbons, along with distinct peaks arising from the aromatic –C=C– units within the dibenzo[*g*,*p*]chrysene core. These features confirm the integrity of the conjugated backbone after framework formation. Elemental composition and chemical bonding states were further examined by XPS and FTIR. The survey XPS spectra (Fig. 1b and S1) confirm the presence of C and Hg elements. The high-resolution C 1s spectrum could be deconvoluted into four components at 284.02 eV (C–Hg, sp), 284.69 eV (C–C, sp^2), 285.33 eV (C–C, sp), and 288.90 eV (C–O), evidencing successful Hg–C bond formation within the framework. The high-resolution spectrum of Hg 4f shows two peaks at 101.08 eV (Hg $4f_{7/2}$) and 105.28 eV (Hg $4f_{5/2}$), confirming the +2-oxidation state of mercury. In the FTIR spectrum (Fig. 1c), the disappearance of the sharp stretching band of terminal alkynes (3310–3370 cm^{-1}) observed in the free TTED ligand verifies the complete consumption of the –C≡CH groups during metal–acetylide coupling.

PXRD patterns (Fig. S2) indicate the semicrystalline nature of TTED-Hg-AF. SEM and TEM images (Fig. 1d and S3) reveal nanosheet-like layered morphologies. Elemental mapping by EDS shows a homogeneous distribution of C and Hg throughout the bulk sample. HRTEM (Fig. 1e and f) reveals an interlayer spacing of 3.62 Å and an in-plane lattice distance of 3.99 nm, collectively corroborating the formation of an ordered 2D network. AFM of exfoliated few-layer TTED-Hg-AF deposited on a Si substrate (Fig. 1g) gives a thickness of approximately 2 nm, corresponding to approximately six stacked layers, confirming its ultrathin 2D character.

Nitrogen adsorption–desorption isotherms (Fig. 1h) demonstrate a Brunauer–Emmett–Teller (BET) specific surface

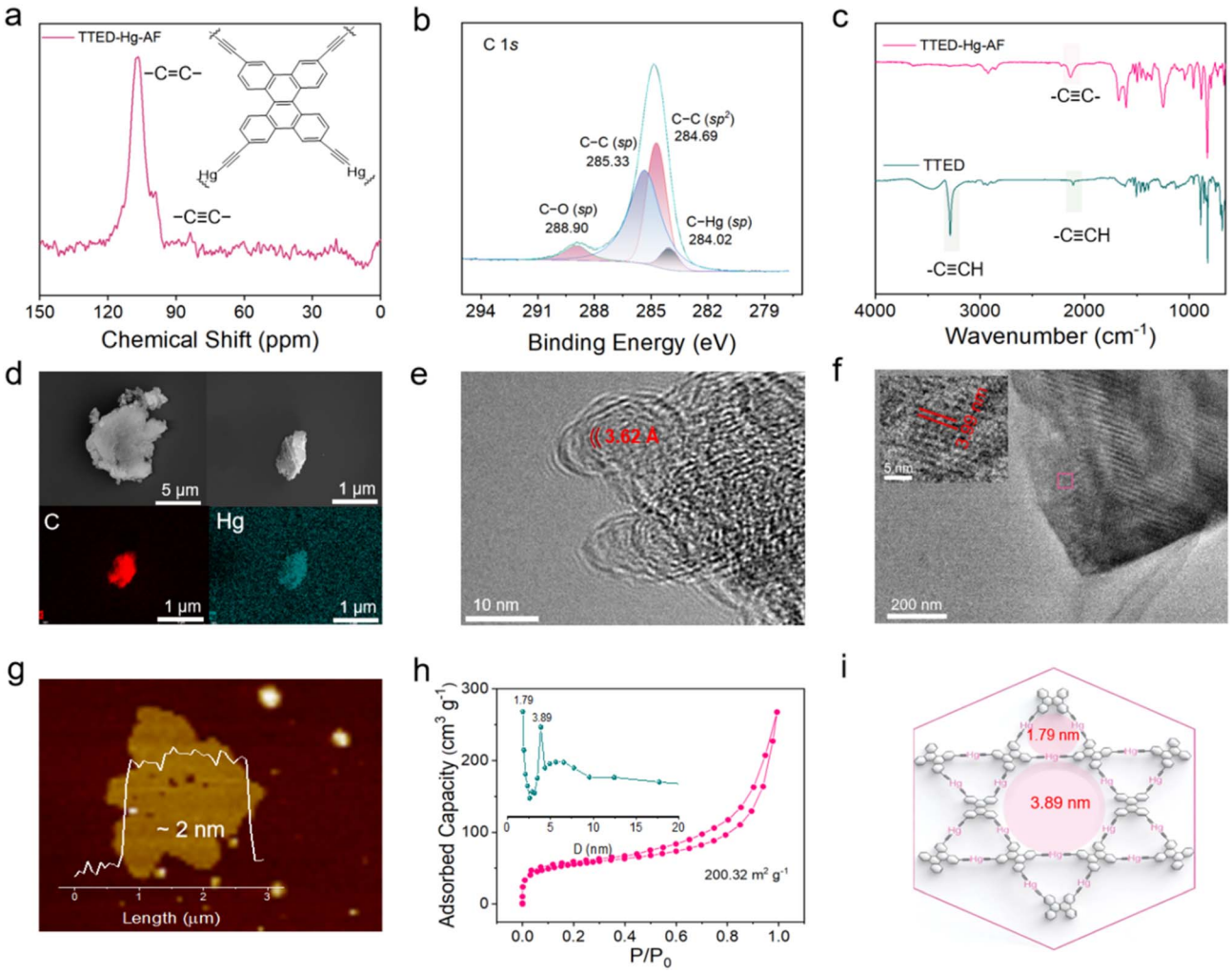

Fig. 1 (a) Solid-state ^{13}C CP-MAS NMR spectrum of TTED-Hg-AF. (b) High-resolution C 1s core-level XPS spectrum of TTED-Hg-AF. (c) FTIR spectra of TTED-Hg-AF and TTED ligand. (d) SEM image and corresponding elemental mapping (C and Hg) of TTED-Hg-AF. (e) HRTEM image showing the interlayer spacing of TTED-Hg-AF. (f) HRTEM image of the lattice fringes of TTED-Hg-AF. (g) AFM image and corresponding height profile of exfoliated TTED-Hg-AF nanosheets. (h) N_2 adsorption–desorption isotherms and corresponding pore size distribution of TTED-Hg-AF. (i) Schematic illustration of the proposed Kagome-type topological structure of the TTED-Hg-AF framework.

area of 200.32 $m^2\ g^{-1}$ and a total pore volume of 0.40 $cm^3\ g^{-1}$. The pore-size distribution shows two distinct microporous and mesoporous regions centered at 1.79 nm (micropores) and 3.89 nm (mesopores), consistent with reported values for dibenzo[*g*,*p*]chrysene-based covalent organic frameworks.[30] These features suggest a Kagome-type topology for TTED-Hg-AF (Fig. 1i) with periodic hexagonal channels. Thermogravimetric analysis (TGA, Fig. S4) indicates an onset decomposition temperature of around 230 °C, confirming the satisfactory thermal stability of the framework.

3.2 Polarization characteristics

The polarization behavior of TTED-Hg-AF was investigated quantitatively using *in situ* KPFM. The measured surface potential (SP) variation reflects the dipole-induced polarization capability-higher SP values indicate stronger intrinsic dipole moments.[31] As shown in Fig. 2a–c, TTED-Hg-AF exhibited an SP of approximately 32 mV in the dark. Under light irradiation, the SP increased to 50 mV, corresponding to an enhancement of 18 mV, while the surface topography remained unchanged (Fig. S5). The increase in SP reflects a downward shift of the local Fermi level toward the conduction band minimum, which is a direct consequence of photogenerated electron accumulation at the surface. Under illumination, electrons are excited from the TTED π-system to the Hg 5d orbitals and alkynyl π* systems, resulting in electron accumulation at the Hg–acetylide catalytic sites and hole accumulation on the organic backbone. This spatial separation is reinforced by the intrinsic dipole moment of the –C≡C–Hg–C≡C– unit, which creates a macroscopic built-in electric field that directs electrons toward the surface. The accumulated electrons form an additional surface dipolar layer, effectively reducing the surface work function and increasing the measured SP. Thus, the observed SP increase serves as a direct experimental signature of the light-enhanced effective dipole field at the TTED-Hg-AF surface.[32] This behavior aligns with previous reports of photo-enhanced polarization in

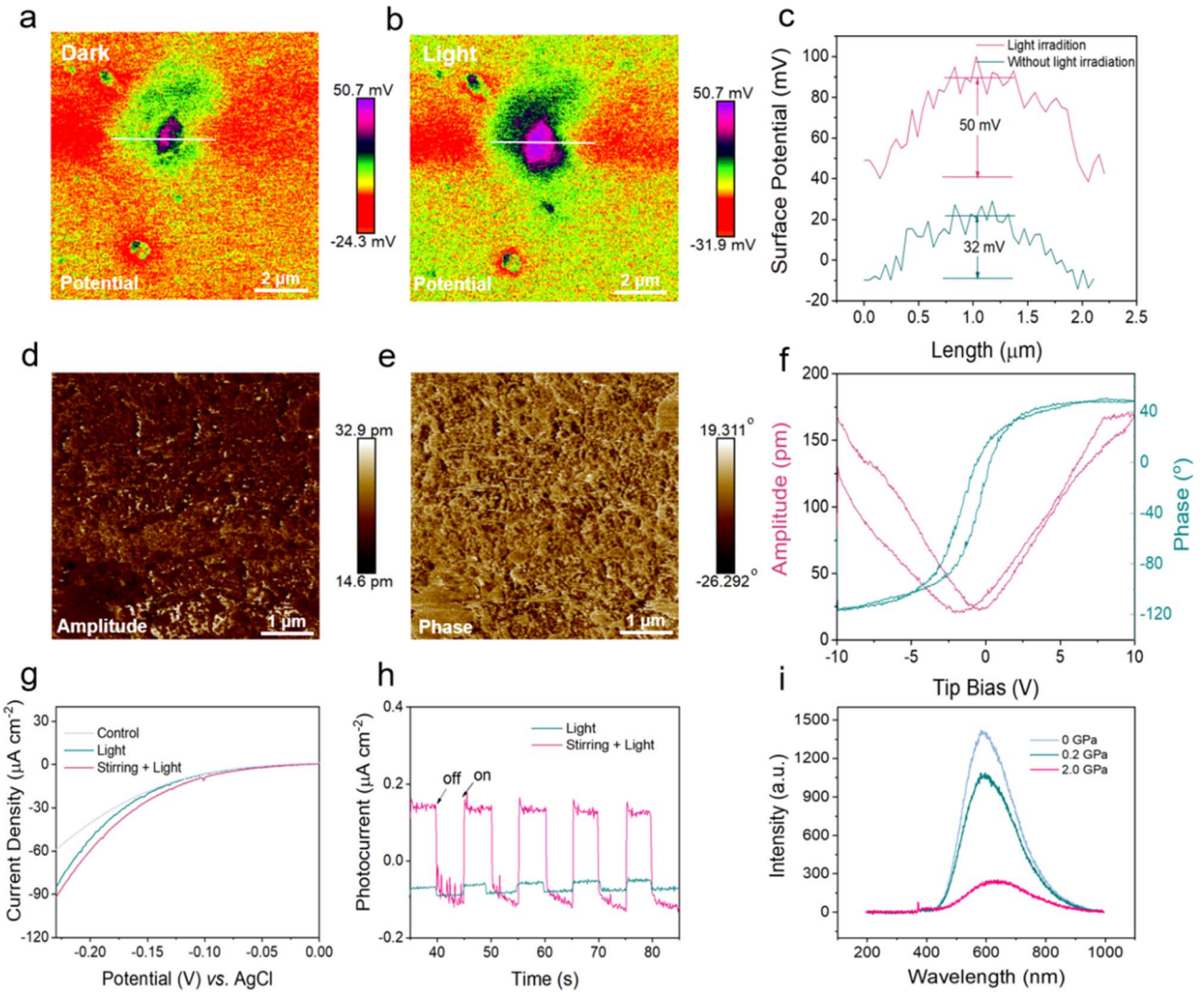

Fig. 2 (a) KPFM surface potential image of TTED-Hg-AF in the dark. (b) Corresponding KPFM image under light irradiation. (c) Differential surface potential map derived from (a) and (b). (d) PFM amplitude image and (e) phase image of TTED-Hg-AF. (f) Piezoelectric hysteresis loops showing phase-voltage and amplitude-voltage characteristics of TTED-Hg-AF. (g) LSV curves of TTED-Hg-AF measured under static conditions, light irradiation, and combined light with mechanical perturbation. (h) Transient photocurrent responses of TTED-Hg-AF under illumination alone and under simultaneous illumination with mechanical stirring. (i) *In situ* high-pressure PL spectra of TTED-Hg-AF under increasing external pressure.

related organometallic frameworks.[33] The pronounced polarization originates from the intrinsic asymmetry of the –C≡C–Hg– linkage. The highly electronegativity of the sp-hybridized carbon withdraws electron density from the Hg center, creating a C(δ^-)–Hg(δ^+) dipole within each repeating unit.[34] These local dipoles align coherently throughout the 2D lattice, establishing a macroscopic built-in electric field across the framework.[35] This internal field acts as a driving force that promotes spatial separation of photogenerated electron–hole pairs, effectively suppressing recombination and directing electrons toward catalytically active Hg sites.

To further probe the intrinsic polarization, PFM was employed to assess the local piezoelectric response.[36] The PFM amplitude correlates with enhanced electron–hole separation and improved charge-transfer kinetics.[37] The obtained amplitude and phase images (Fig. 2d–f and S6) reveal well-defined ferroelectric domains with distinct contrast, corresponding to regions of opposite polarization orientation. The phase-voltage and amplitude-voltage hysteresis loops show a nearly 180° phase reversal and a characteristic butterfly-shaped amplitude profile (Fig. 2f), providing clear evidence of switchable piezoelectric domains and spontaneous polarization in TTED-Hg-AF.

Complementary *in situ* analyses, including high-pressure PL, transient photocurrent, and linear sweep voltammetry (LSV) (Fig. 2g–i), further support the role of polarization in enhancing charge dynamics. LSV measurements (Fig. 2g) show that at an overpotential of −0.23 V, the current densities reach −60 μA, −83 μA, and −90 μA under static conditions, light irradiation, and combined light plus external force, respectively. The transient photocurrent response (Fig. 2h) is markedly enhanced under external mechanical perturbation. *In situ* high-pressure PL spectra (Fig. 2i) exhibit a substantial decrease in intensity

and a pronounced red-shift with increasing pressure, indicating suppressed charge recombination. The observed red-shift is attributed primarily to pressure-enhanced π–π stacking interactions.[38] These findings demonstrate that the built-in electric fields, further amplified by vibration, significantly promotes charge-carrier separation and transfer.

3.3 Photocatalytic CO_2 reduction performance

The electronic structure of TTED-Hg-AF was characterized by UV-vis DRS, Mott–Schottky analysis, and valence-band XPS spectroscopy (VB-XPS) (Fig. 3a, b and S7). The DRS spectrum exhibits broad absorption from 250 to 550 nm, enabling visible-light harvesting for CO_2 reduction. The Tauc plot gives an optical bandgap of 2.57 eV. The flat-band potential derived from Mott–Schottky measurements is −0.34 V *vs.* NHE, and the valence-band maximum obtained from VB-XPS is +1.20 eV. Accordingly, the corresponding conduction band (CB) potential is calculated to be −1.37 eV *vs.* NHE, which is thermodynamically favorable for the reduction of CO_2 to CO (−0.53 eV *vs.* NHE) (Fig. S8). CO_2 adsorption isotherms further confirm the framework's affinity toward CO_2, with uptake capacities of 179.26 $m^2\ g^{-1}$ at 273 K and 190.62 $m^2\ g^{-1}$ at 298 K (Fig. 3c). These data indicate strong CO_2 adsorption under static conditions. However, the exceptional catalytic activity of TTED-Hg-AF primarily arises from dynamic polarization-assisted CO_2 activation rather than adsorption equilibrium alone.[39]

Owing to its extended π-conjugated structure and strong local polarization, TTED-Hg-AF was evaluated as a piezo-photocatalyst for CO_2 reduction reaction (CO_2RR) under visible light (λ > 420 nm, 100 mW cm^{-2}) and ultrasonic irradiation (100 W). The reactions were conducted in CO_2-saturated aqueous solution containing TEOA as a sacrificial donor and $[Ru(bpy)_3]Cl_2$ as a photosensitizer. Under light irradiation alone, the CO yield reached 1.60 μmol g^{-1} h^{-1} with 100%

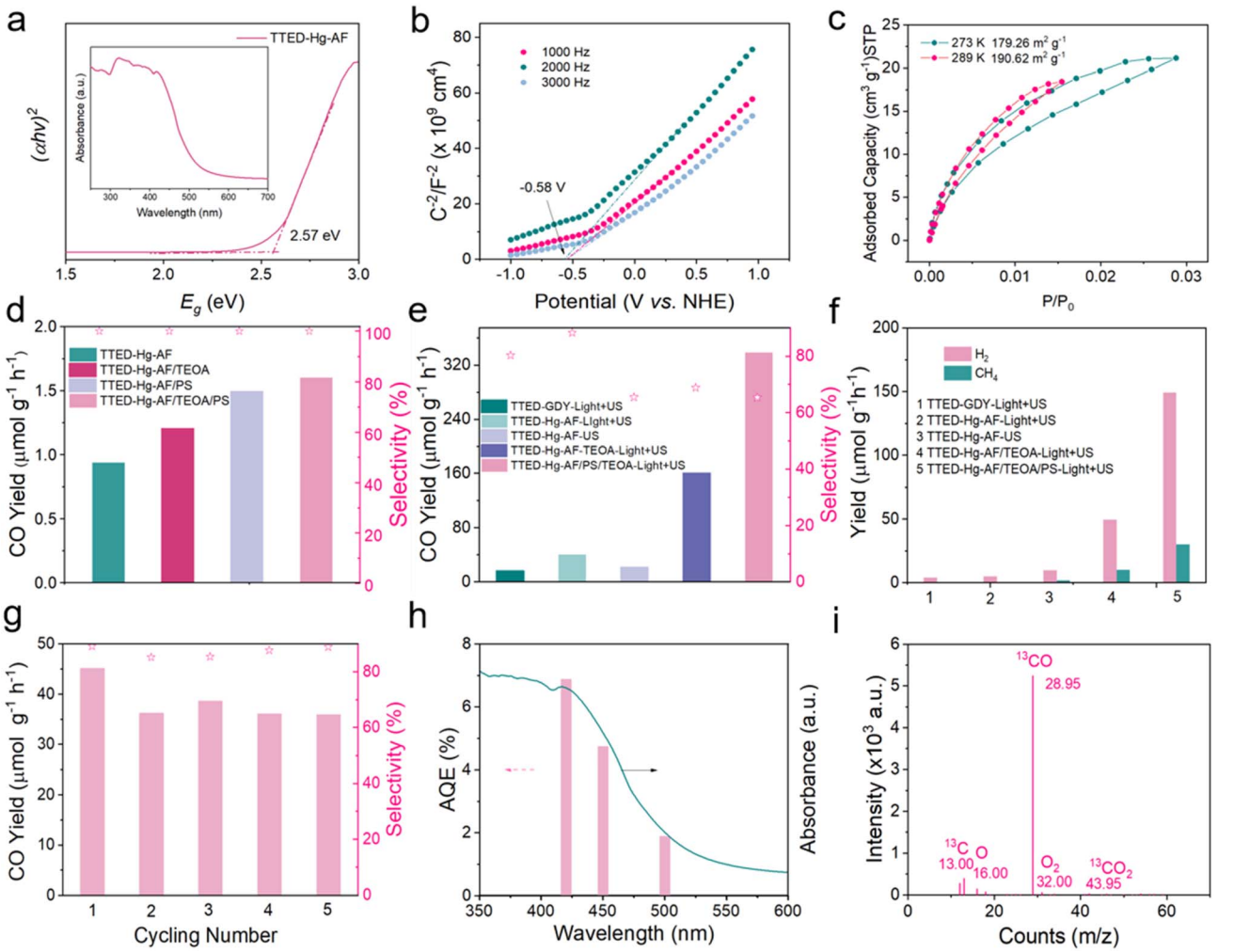

Fig. 3 (a) UV-vis DRS spectrum (inset) and corresponding Tauc plot for optical bandgap determination of TTED-Hg-AF. (b) M–S plots of TTED-Hg-AF measured at various frequencies. (c) CO_2 adsorption isotherms of TTED-Hg-AF at 273 K and 289 K. (d) Comparative CO evolution rates for various catalytic systems under light irradiation. (e) Comparative CO evolution rates for various catalytic systems under simultaneous ultrasound and light irradiation. (f) Comparative H_2 and CH_4 evolution rates for various catalytic systems under combined ultrasound and light irradiation. (g) Cycling stability test of TTED-Hg-AF over five consecutive runs under combined ultrasonic and light irradiation. (h) AQE of TTED-Hg-AF at 420, 450, and 500 nm under combined light and ultrasound irradiation. (i) GC-MS analysis confirming ^{13}CO isotope labeling experiment.

selectivity when both TEOA and the PS were present (Fig. 3d). TEOA enhances charge separation and transfer efficiency,[40,41] while the PS facilitates electron injection from photoexcited $[Ru(bpy)_3]^{2+}$ to the conduction band of TTED-Hg-AF.[42] PL spectra (Fig. S9) further confirm prolonged charge-carrier lifetimes in the presence of TEOA and PS, indicating their synergistic role in boosting photocatalytic activity.

To probe the influence of the polarization field on CO_2RR, an external ultrasonic (US) field was applied to induce piezoelectric polarization (Fig. 3e, f and S10).[23,43] Under US irradiation alone, TTED-Hg-AF produced 21.82 μmol g^{-1} h^{-1} of CO with 65.32% selectivity, along with 1.65 μmol g^{-1} h^{-1} of CH_4. No other liquid carbon products were generated (Fig. S11). Combining light and ultrasound yielded a synergistic enhancement: CO production increased to 40.38 μmol g^{-1} h^{-1} with 88.27% selectivity, demonstrating that external mechanical perturbation also improves CO selectivity. In the TTED-Hg-AF/TEOA system under combined ultrasound and light irradiation, the CO yield reached 160.57 μmol g^{-1} h^{-1} with 64.65% selectivity and CH_4 generation was 16.06 μmol g^{-1} h^{-1}. The addition of TEOA effectively suppressed electron–hole recombination (Fig. S12). When both TEOA and PS were introduced, the yields further increased to 338.57 μmol g^{-1} h^{-1} for CO and 30.15 μmol g^{-1} h^{-1} for CH_4 while maintaining ~65% CO selectivity under simultaneous US and light irradiation. The moderate increase in H_2 yield (149.39 μmol g^{-1} h^{-1}) under ultrasound arises from improved overall charge separation efficiency, which increases the total electron flux. However, CO selectivity remains high because the –C≡C–Hg–C≡C– sites intrinsically favor CO_2 activation over proton reduction. For comparison, the Hg-free analogue TTED-GDY produced only 16.74 μmol g^{-1} h^{-1} of CO with 80.33% selectivity, confirming that the introduction of Hg

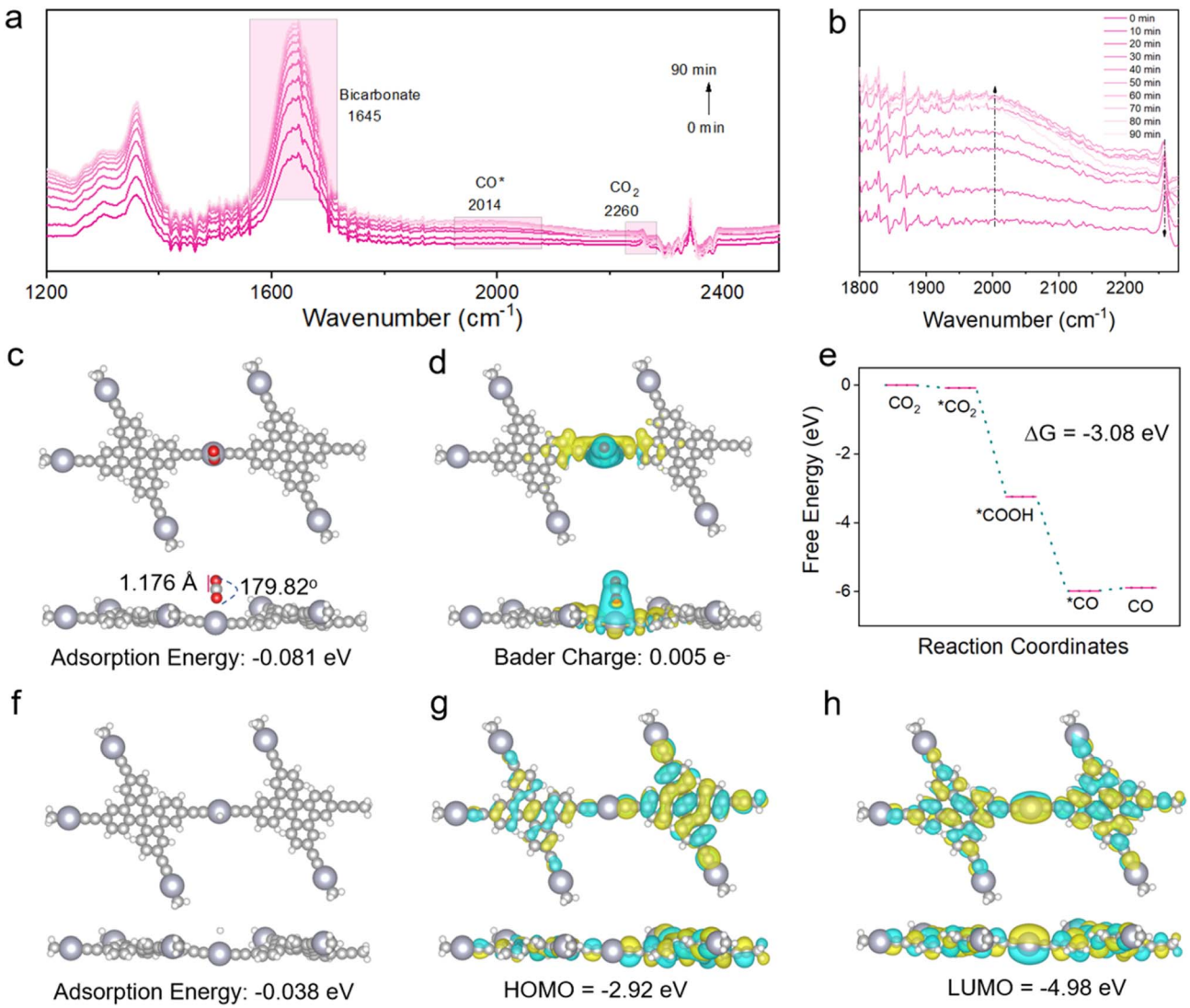

Fig. 4 (a) Time-dependent *in situ* DRIFTS spectra recorded during photocatalytic CO_2 reduction on TTED-Hg-AF. (b) Magnified view of the 1800–2350 cm^{-1} region highlighting the evolution of key intermediate bands. (c) Optimized DFT geometries and corresponding adsorption energies for CO_2 on TTED-Hg-AF. (d) Charge-density difference isosurfaces (yellow: charge accumulation, cyan: depletion) and Bader charge analysis for adsorbed CO_2. (e) Gibbs free-energy diagram for the CO_2-to-CO conversion pathway on TTED-Hg-AF. (f) Optimized DFT geometries and adsorption energies for H adsorption on TTED-Hg-AF. (g) HOMO and (h) LUMO distributions of TTED-Hg-AF.

centers significantly enhances both activity and product selectivity. These findings indicate that ultrasonic-assisted photocatalysis amplifies the intrinsic polarization of TTED-Hg-AF, thereby promoting directional charge separation and accelerating surface redox kinetics.

The catalyst exhibited stable performance over multiple cycles, with nearly constant CO production rates and selectivity (Fig. 3g). Post-reaction XRD, FTIR, and XPS analyses (Fig. S13–S15) revealed negligible structural or compositional changes. The Hg^{II} leaching amount after reaction is 0.056 ppm, which is also acceptable for laboratory-scale catalytic processes (Fig. S16). A positive shift in the Hg 4f binding energy after reaction suggests electron-density depletion at the Hg^{II} centers during CO_2 reduction, verifying their direct involvement in catalytic electron transfer through the conjugated network.

The apparent quantum efficiency (AQE) of TTED-Hg-AF was evaluated under monochromatic light (Fig. 3h and S17). The AQE reached 0.186% at 420 nm under light alone, which dramatically increased to 6.87% under combined light and ultrasonic stimulation—representing a 37-fold enhancement. This substantial improvement underscores the critical role of piezoelectric polarization in promoting charge separation and lowering kinetic barriers in CO_2RR. Isotopic tracing experiments using $^{13}CO_2$ as the feed gas confirmed the carbon origin of the products. The main GC-MS signals at m/z = 28.95, 13.0, and 16.0 correspond to ^{13}CO, ^{13}C, and O, respectively. Minor peaks at m/z = 44 (^{13}CO) and m/z = 32 (O_2) originate from residual feed gas and air (Fig. 3i and S18), unambiguously verifying that CO is generated from CO_2 rather than from other carbon sources.

3.4 Catalytic mechanism

The photocatalytic CO_2 reduction mechanism was investigated by *in situ* DRIFTS (Fig. 4a and b). Upon continuous CO_2 flow under illumination, a band at 1645 cm^{-1}, assigned to the C–O–C stretching vibration of bicarbonate species, progressively intensified. Meanwhile, the intensity of the gas-phase CO_2 peak at 2260 cm^{-1} decreased with the emergence of a new band at 2024 cm^{-1}, corresponding to adsorbed CO* species. These spectral changes clearly indicate the conversion of CO_2 to CO on the surface of TTED-Hg-AF. Although the characteristic *COOH intermediate signal overlaps with the broad O–C–O vibration region, the overall spectral evolution supports a CO_2 → *COOH → CO reaction pathway. CO_2 adsorption and activation were further examined using DFT calculations. The optimized adsorption configuration and the corresponding charge-density difference plots are depicted in Fig. 4c, d, and S19. The calculated adsorption energy (ΔE_{ads}) of −0.081 eV suggests a physisorption-dominated process with mild activation. Upon adsorption, the CO_2 molecule adopts a slightly bent geometry (O–C–O angle = 179.82°) with elongated C–O bonds (1.176 Å), indicative of charge transfer into the antibonding $2\pi_\mu$ orbitals. Differential charge-density analysis confirms that CO_2 preferentially binds to the –C≡C–Hg–C≡C– motifs, and Bader charge analysis reveals a transfer of ~0.005e^- from the framework to CO_2. These results identify the –C≡C–Hg–C≡C– linkages as the primary adsorption and activation sites, enabling π–d–π orbital interactions between CO_2 and the Hg centers.[20]

The Gibbs free-energy profile for the elementary CO_2 reduction steps is summarized in Fig. 4e. The reaction proceeds as CO_2 → *CO_2 → *COOH → *CO → CO. All steps are thermodynamically favorable,[44] with the formation of *COOH identified as the potential-limiting step with a ΔG of −3.08 eV. Thus, the Hg^{II}-bis(acetylide) units serve as efficient catalytic centers that stabilize the *COOH intermediate and facilitate subsequent CO desorption. Following *COOH formation, proton–electron coupling yields *CO and H_2O, after which *CO readily desorbs from the framework surface.

The –C≡C–Hg–C≡C– fragments allow strong lateral overlap between filled Hg 5d orbitals (especially d_{xz} and d_{yz}) and the π* orbitals of the adjacent acetylide groups.[45,46] This orbital hybridization confers a dual electronic advantage: (1) a conductive σ-framework that promotes rapid longitudinal electron transport. (2) A d_π–p_π* back-donation mechanism that modulates electron density at the Hg site, thereby balancing CO_2 adsorption strength and product release.[47,48] Moreover, the calculated hydrogen adsorption energy (ΔE_H = −0.038 eV, Fig. 4f) indicates that H^+ activation is less favorable than CO_2 activation at the –C≡C–Hg–C≡C– sites, which accounts for the high CO selectivity and suppressed competing hydrogen evolution reaction (HER).

To visualize electron-transfer pathways, the frontier molecular orbital distributions of TTED-Hg-AF were analyzed (Fig. 4g and h). The highest occupied molecular orbital (HOMO) is predominantly localized on the TTED ligand, while the lowest unoccupied molecular orbital (LUMO) resides on the –C≡C–Hg–C≡C– segments. The calculated HOMO–LUMO gap (ΔE = 2.06 eV) aligns well with the experimental bandgap, supporting a ligand-to-metal charge transfer (LMCT) mechanism. Under photoexcitation, electrons are promoted from the TTED π-system to the Hg 5d orbitals, enabling efficient charge separation and facilitating CO_2 reduction through a polarization-assisted LMCT process.

The overall catalytic mechanism, illustrated in Fig. 5, operates through distinct functional components: the dibenzo[*g*,*p*]chrysene linkers act as an electron reservoir that shuttles charge to the Hg-bis(acetylide) catalytic moieties, where CO_2 reduction to CO takes place. Electron donation is facilitated by TEOA as

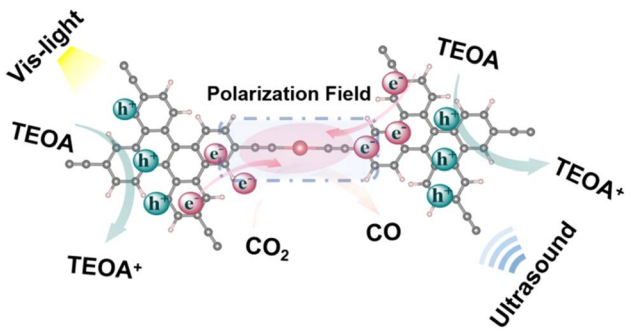

Fig. 5 Schematic illustration of the proposed mechanism for ultrasound-enhanced photocatalytic CO_2 reduction over TTED-Hg-AF.

a sacrificial reductant. This process is significantly enhanced by the polarized electric field generated by the –C≡C–Hg–C≡C– units, which accelerates the separation and interfacial transfer of photogenerated charge carriers. Ultimately, the combined inputs of light and ultrasound synergistically drive the enhanced CO_2 conversion.

4. Conclusion

In summary, we developed a novel 2D Hg^{II}–acetylide framework (TTED-Hg-AF) featuring orbital hybridization and an intrinsic dipole field, which exhibits exceptional photocatalytic activity for CO_2 reduction. Under the synergistic action of visible-light irradiation and ultrasonic excitation, TTED-Hg-AF achieved a remarkable CO production rate of 338.57 μmol g^{-1} h^{-1} with 65.35% selectivity, accompanied by a CH_4 yield of 30.15 μmol g^{-1} h^{-1}. In contrast, under light irradiation alone, the activity was significantly lower (1.60 μmol g^{-1} h^{-1} with 100% selectivity), highlighting the essential role of ultrasonic enhanced polarization in boosting charge separation and catalytic performance. Through comprehensive characterization—including *in situ* DRIFTS, PFM, KPFM, and DFT calculations—we identified that photoexcited electrons from the TTED ligand are efficiently transferred to the –C≡C–Hg–C≡C– linkages. These linear motifs act as the primary catalytic sites, effectively capturing and activating CO_2 molecules and reducing the energy barrier for the formation of the *COOH intermediate. Furthermore, the built-in polarization field, which is amplified under ultrasonic stimulation, promotes directional charge transport, accelerates electron–hole separation, and enhances overall redox efficiency. This work establishes Hg^{II}–acetylide frameworks as a promising new class of 2D photocatalysts that uniquely combine extended structural conjugation, d_π–p_π electronic coupling, and intrinsic polarization engineering. The design strategy presented here offers a versatile pathway for constructing next-generation 2D materials with enhanced internal electric fields, providing a robust platform for efficient solar-to-chemical energy conversion.

Author contributions

Mude Zhu: conceptualization, methodology, data acquirement, writing – original draft preparation. Muchun Xu: BET data acquirement, review & editing. Lincan Fang: conceptualization, DFT calculation, review & editing. Linli Xu: supervision, resources, project administration, writing – review & editing.

Conflicts of interest

There are no conflicts to declare.

Data availability

The data supporting this article have been included as part of the supplementary information (SI). Supplementary information: SEM, XPS, DFT calculation and further experimental details. See DOI: https://doi.org/10.1039/d6ta01264g.

Acknowledgements

L. L. X. thanks The Hong Kong Research Grants Council (PolyU 25301524; Young Collaborative Research Grant C5001-24), Shenzhen Science and Technology Program (JCYJ20250604185428038), Guangdong Provincial Natural Science Foundation-General Project (2024A1515010422), and PolyU (CE2N, CDB5, CE35, CE01, CDDA, CEE7).

References

1 Q.-J. Wu, J. Liang, Y.-B. Huang and R. Cao, *Acc. Chem. Res.*, 2022, **55**, 2978–2997.
2 Y.-H. Luo, L.-Z. Dong, J. Liu, S.-L. Li and Y.-Q. Lan, *Coord. Chem. Rev.*, 2019, **390**, 86–126.
3 J. Liang, H. Yu, J. Shi, B. Li, L. Wu and M. Wang, *Adv. Mater.*, 2023, **35**, 2209814.
4 Y. Zhou, Z. Wang, L. Huang, S. Zaman, K. Lei, T. Yue, Z. a. Li, B. You and B. Y. Xia, *Adv. Energy Mater.*, 2021, **11**, 2003159.
5 W. Che, S. Zhao, W. J. Byun, T. Tao, J. P. Jeon, Q. Zhao, Y. Shao, J. Li, J. Kim, J. S. Lee and J.-B. Baek, *Adv. Mater.*, 2025, **37**, e06961.
6 C.-L. Ho and W.-Y. Wong, *Coord. Chem. Rev.*, 2013, **257**, 1614–1649.
7 W.-Y. Wong and C.-L. Ho, *Coord. Chem. Rev.*, 2006, **250**, 2627–2690.
8 M. Zhu, H. Su, F. Yang, Y. Qin, F. C.-H. Hui, R. Zhang, J. Geng, K. Wang, X. Fan, W.-Y. Wong and L. Xu, *J. Am. Chem. Soc.*, 2025, **147**, 29192–29204.
9 A. B. Shaff, A. Hazra, B. W. Gardner and G. Lalic, *J. Am. Chem. Soc.*, 2024, **147**, 27–32.
10 Y. Qin, Y. Wang, J. Lu, L. Xu and W. Y. Wong, *Angew. Chem., Int. Ed.*, 2025, **64**, e202418269.
11 C. Zhang, Y. Qin, J. Li, L. Xu and W.-Y. Wong, *Appl. Catal., B*, 2025, **379**, 125689.
12 H. Si, M. Zhu, Z. Li, J. Wang, J. Li, L. Xu, H. Huang, Y. Liu, W.-Y. Wong and Z. Kang, *Chem. Eng. J.*, 2025, **516**, 163963.
13 Y. Qin, J. Lu, C. Zhang, L. Xu and W. Y. Wong, *Angew. Chem., Int. Ed.*, 2025, **64**, e202505883.
14 Q. Wang, H. Si, A. A. Sergeev, J. Li, Z. Li, Y. Wang, T. Long, K. S. Wong, L. Xu, Z. Kang and W.-Y. Wong, *Nano Energy*, 2025, **136**, 110685.
15 M. Wilhelm, S. Deeken, E. Berssen, W. Saak, A. Lützen, R. Koch and H. Strasdeit, *Eur. J. Inorg. Chem.*, 2004, **2004**, 2301–2312.
16 X. Yan, J. Zhu, Y. Liu, Y. Liu, H. He, C. Xu, S. Yang, Q. Ji, K. Wang and S. Liu, *J. Mater. Chem. A*, 2025, **13**, 4948–4959.
17 Y. Lei, X. Sala, J. García-Antón and J. Muñoz, *J. Mater. Chem. A*, 2025, **13**, 12712–12745.
18 J. G. Melnick and G. Parkin, *Science*, 2007, **317**, 225–227.
19 L. Xu, J. Sun, T. Tang, H. Zhang, M. Sun, J. Zhang, J. Li, B. Huang, Z. Wang, Z. Xie and W.-Y. Wong, *Angew. Chem., Int. Ed.*, 2021, **60**, 11326–11334.
20 M. Fang, L. Xu, H. Zhang, Y. Zhu and W.-Y. Wong, *J. Am. Chem. Soc.*, 2022, **144**, 15143–15154.
21 S. Ahmed, L. Xu, M. N. A. S. Ivan, M. Zhu, Y. Qin, M. Sun, S. Saha, Y. Shafayet, B. Huang and W.-Y. Wong, *Carbon*, 2025, **238**, 120234.

22 K. Wang, Z. Guan, Y. He and M. Fan, *Nano Energy*, 2025, **133**, 110518.
23 Z. Li, Y. Zhou, Y. Zhou, K. Wang, Y. Yun, S. Chen, W. Jiao, L. Chen, B. Zou and M. Zhu, *Nat. Commun.*, 2023, **14**, 5742.
24 H. Hu, X. Li, K. Zhang, G. Yan, W. Kong, A. Qin, Y. Ma, A. Li, K. Wang and H. Huang, *Adv. Mater.*, 2025, **37**, 2419023.
25 M. L. Xu, M. Lu, G. Y. Qin, X. M. Wu, T. Yu, L. N. Zhang, K. Li, X. Cheng and Y. Q. Lan, *Angew. Chem., Int. Ed.*, 2022, **134**, e202210700.
26 X. A. Li, Y. Wang, Z. Z. Liang, X. B. Peng, L. M. Xiao, L. Gong, X. Yang, B. Zou, Y. Zhou and J. M. Liu, *Adv. Sci.*, 2026, e23030.
27 D. Cao, C. Gong, Y. Han, C. Zhu, Y. Ma, Q. Xia, Y. Peng and G. Yuan, *Angew. Chem., Int. Ed.*, 2025, **64**, e202516908.
28 Q. Ge and M. Neurock, *J. Phys. Chem. B*, 2006, **110**, 15368–15380.
29 Y. Gauthier, M. Schmid, S. Padovani, E. Lundgren, V. Buš, G. Kresse, J. Redinger and P. Varga, *Phys. Rev. Lett.*, 2001, **87**, 036103.
30 J. J. Yu, X. Huang, L. Y. Wang, Y. Z. Wu, Z. W. Huang, L. L. Su, N. N. Wang, J. P. Yu and W. Q. Shi, *Adv. Mater.*, 2025, **37**, e04808.
31 Y. Liu, X. Deng, Z. Wang, S. F. Yin and P. Chen, *Angew. Chem., Int. Ed.*, 2025, **64**, e202516117.
32 J. Lin, J. Liu, K. Zhang, Y. Deng, W. Che, X. Pang, Q. Zhang, W. Cai, Z. Zeng and N. Wu, *Adv. Funct. Mater.*, 2025, e20336.
33 Z. Meng, J. Zhang, H. Long, H. García, L. Zhang, B. Zhu and J. Yu, *Angew. Chem., Int. Ed.*, 2025, e202505456.
34 J. Gao, X. Yan, X. Gu, X. Fu, Q. Chang, Z. Zhang, Y. Wang, C. Huang and Y. Li, *J. Am. Chem. Soc.*, 2024, **146**, 27030–27039.
35 Y. Ma, C. Gan, L. Liu, J. Pan, H. Rong, Y. Guo, Y. Yuan and N. Wang, *Adv. Funct. Mater.*, 2025, e23125.
36 Z. Wang, D. Zhou, K. Tian, G. Chen, Y. Li, S. F. Liu, S.-T. Lee, Y. Ji and J. Yan, *Nat. Commun.*, 2025, **16**, 11066.
37 W. Zheng, Y. Tang, C. Jia, Z. Liu, Z. Zhang and K. Zhao, *J. Mater. Chem. A*, 2024, **12**, 11378–11389.
38 C. Liu, G. Xiao, M. Yang, B. Zou, Z. L. Zhang and D. W. Pang, *Angew. Chem., Int. Ed.*, 2018, **57**, 1893–1897.
39 L. Liu, Q. An, X. Zou, Y. Zha, G. Zhao, Q. Liu, L. Duan and H. Guo, *Appl. Catal., B*, 2025, 125915.
40 R. Das, S. Chakraborty and S. C. Peter, *ACS Energy Lett.*, 2021, **6**, 3270–3274.
41 C. R. Carr, M. A. Vrionides, I. S. Sosulin, A. Lisouskaya, M. Z. Ertem and D. C. Grills, *J. Am. Chem. Soc.*, 2025, **147**, 32005–32014.
42 N.-Y. Huang, H. He, S. Liu, H.-L. Zhu, Y.-J. Li, J. Xu, J.-R. Huang, X. Wang, P.-Q. Liao and X.-M. Chen, *J. Am. Chem. Soc.*, 2021, **143**, 17424–17430.
43 H. Sudrajat, I. Rossetti and J. C. Colmenares, *J. Mater. Chem. A*, 2023, **11**, 24566–24590.
44 Y. N. Gong, J. H. Mei, W. J. Shi, J. W. Liu, D. C. Zhong and T. B. Lu, *Angew. Chem., Int. Ed.*, 2024, **136**, e202318735.
45 M. Kurihara and H. Nishihara, *Coord. Chem. Rev.*, 2002, **226**, 125–135.
46 Z. Qian, G. Han, Y. Tan, N. Ye, S. Wang, Z. Lin, Q. Huang, Y. Gu, H. Guo, F. Liu, K. Wang, L. Li, C. Shang, M. Luo and S. Guo, *Nat. Commun.*, 2025, 11265.
47 Z. Zhang, Z. Zhang, M. Xie, R. Tian, C. Chai, R. Xu, X.-b. Chen, Y. Song, H. Lu, Z. Shi and S. Feng, *CCS Chem.*, 2025, **7**, 867–882.
48 W. Zhong, R. Sa, L. Li, Y. He, L. Li, J. Bi, Z. Zhuang, Y. Yu and Z. Zou, *J. Am. Chem. Soc.*, 2019, **141**, 7615–7621.

